

Phenomenology of bubble-collapse-driven penetration of biomaterial-surrogate liquid-liquid interfaces

Shucheng Pan, Stefan Adami,* Xiangyu Hu, and Nikolaus A. Adams
*Chair of Aerodynamics and Fluid Mechanics, Department of Mechanical Engineering,
Technical University of Munich, 85748 Garching, Germany*



(Received 26 March 2018; published 27 November 2018)

The paper presents phenomenology of interaction and penetration of liquid-liquid material interfaces initiated by shock-driven collapse of single and multiple microbubbles situated near the material interface. Previous experimental studies have established such a generic setting as relevant for the investigation of sonoporation, i.e., the perforation of live cells by microbubble collapses. We consider a planar or spherical, single- or dual-layer, material interface between a gelatin material and water. A single or several ideal-gas microbubbles are positioned near the interface. Bubble collapse is initiated by a shock wave with a pressure profile specific to laser generation and is flat when hitting the gas-water interface. The interfacial acoustic impedance match singles out the collapse-induced re-entrant jet as main event. High-resolution sharp-interface numerical methods are employed to ensure that wave dynamics, hydrodynamics, and interface transporting are accurately resolved. Bubble configurations are varied between single and double and between attached and with standoff distance. Parameters varied are shock-wave peak pressure and viscosity ratio between single and double layers of gelatin and the surrounding water. For inertia-dominated cases, two regimes are observed, the first characterized by linear growth of the penetration depth and the second by a $t^{2/3}$ scaling. The latter range is affected by viscosity which reduces penetration speed. The results show that process parameters, in particular shock overpressure, control not only penetration depth but also the size of the interface perforation, indicating means to steer processes in biomedical applications.

DOI: [10.1103/PhysRevFluids.3.114005](https://doi.org/10.1103/PhysRevFluids.3.114005)

I. INTRODUCTION

Fluid dynamics is essential to biotechnological processes and biomedical therapies [1]. An important example is extracorporeal shockwave lithotripsy (ESWL) [2], side effects of which have stimulated other therapeutical approaches to improve drug delivery or noninvasive cancer treatment [3]. The underlying mechanism of ESWL is shock-driven microbubble collapse, whose wave-dynamic and hydrodynamic effects initiate calculi fragmentation, cell membrane rupture [4], and tissue damage [5–10]. Among the most promising shock-interaction-driven biomedical phenomena is sonoporation, where acoustic cavitation of microbubbles leads to temporary small-scale cell-membrane perforations accompanied by jetting of extracellular liquid into the cell [11–15].

*stefan.adami@aer.mw.tum.de

Published by the American Physical Society under the terms of the [Creative Commons Attribution 4.0 International](https://creativecommons.org/licenses/by/4.0/) license. Further distribution of this work must maintain attribution to the author(s) and the published article's title, journal citation, and DOI.

Microbubble collapses near the interface between liquid and cell membrane generate collapse shock and re-entrant jet. The collapse shock typically has higher intensity than the precursor shockwave initiating bubble collapse and hits the target material much more localized. At the same time, a re-entrant liquid jet toward the interface is generated, induced by the nonspherical bubble collapse. It is known that both effects can damage the cell membrane; however, the precise mechanisms are unclear and motivate our investigation. Gas or vapor bubble collapse in bulk fluid or near material interfaces and with interface interactions has been studied intensely, e.g., in Refs. [6,7,16–18]. Much less is known, however, about the details of the interface-penetration processes induced by bubble collapse. To address this issue, we consider in this paper a generic configuration that follows the experimental work of Ref. [9]. Gelatin is used as surrogate for the cell-interior material. The extracellular liquid is modeled as water, and the bubble material is ideal gas. With this choice, the liquid-gelatin interface is transparent with respect to the shock, and the interaction with the interface is hydrodynamic only. We extend the experimental configuration by considering also spherical interfaces, where surface tension serves to mimic the effect of cell membrane, cell cortex, and cytoskeleton [19]. Moreover, the effects of another cellular-material layer in a compound cell model [20] and of bubble-bubble interactions are investigated. As experimental access even for laboratory generic configurations cannot provide fully detailed information on wave dynamics and hydrodynamic fields, we employ a state-of-the-art high-resolution numerical method for conservative multimaterial interface interaction [21].

The paper is structured as follows. The physical model and configurations are discussed in Secs. II and III, respectively. In Sec. IV, the numerical method with the multimaterial sharp-interface treatment is detailed. Then, the bubble collapse, re-entrant jet formation, and penetration process are investigated for the planar interface in Sec. V and for spherical material interfaces in Sec. VI. Finally, conclusions are drawn in Sec. VII.

II. PHYSICAL MODEL

We assume all involved materials to be immiscible (weakly) compressible fluids whose evolution is described by the mass, momentum, and energy conservation equations,

$$\begin{aligned} \rho_t + \nabla \cdot (\rho \mathbf{u}) &= 0, \\ (\rho \mathbf{u})_t + \nabla \cdot (\rho \mathbf{u} \otimes \mathbf{u}) &= -\nabla p + \nabla \cdot \boldsymbol{\tau} + \sigma \kappa \delta \mathbf{n}, \\ (\rho E)_t + \nabla \cdot [(\rho E + p) \mathbf{u}] &= \nabla \cdot (k \nabla T) + \nabla \cdot (\boldsymbol{\tau} \mathbf{u}) + \sigma \kappa \delta \mathbf{u} \cdot \mathbf{n}, \end{aligned} \quad (1)$$

where ρ is the mass density, p is the pressure, \mathbf{u} is the velocity vector, T is the temperature, and E is the total energy density. The surface-tension coefficient σ is defined at material interfaces: between gas (“g”) and liquid (“l”) $\sigma_{g,l} = 0.073 \text{ Nm}^{-1}$, between liquid and cell (“c1”) $\sigma_{l,c1} = 2.4 \times 10^{-5} \text{ Nm}^{-1}$, and between cell and cell core (“c2”) $\sigma_{c1,c2} = 2.4 \times 10^{-5} \text{ Nm}^{-1}$, according to Ref. [22]. The curvature κ is calculated following Ref. [23]. δ is the Dirac δ function centered at the respective material interface, and \mathbf{n} is the interface normal direction. k is the thermal conductivity, and $\boldsymbol{\tau}$ is the viscous stress tensor. As the materials are treated as Newtonian fluids, $\boldsymbol{\tau} = -2/3 \mu \nabla \cdot \mathbf{u} \mathbf{I} + \mu (\nabla \mathbf{u} + \nabla \mathbf{u}^T)$, where \mathbf{I} is the unit tensor. The effect of surface-tension force $\sigma \kappa \delta \mathbf{n}$ and its work $\sigma \kappa \delta \mathbf{u} \cdot \mathbf{n}$ are considered by a balanced-force formulation [23] within the Riemann problem at the interface; see Sec. IV D for details. Following Refs. [7,24], we use a stiffened-gas equation of state [25] that applies to all materials $p(\rho, e) = (\gamma - 1)\rho e - \gamma B$, where e is the internal energy density, γ is the ratio of specific heats, and the parameter B accounts for the material stiffness; see Table I. Heat conduction is considered as negligible due to the small physical timescales (in the range of microseconds), and mass diffusion and phase transfer also can be neglected [6]. The employed sharp-interface method [21] can handle complex interface topology changes.

TABLE I. Material properties (heat capacity ratio γ and material stiffness B) and initial conditions (density ρ , pressure p , bulk velocity \mathbf{u}) for gas bubble, tissuelike material, cell model, pre- and postshocked ambient liquid [22].

Materials	γ	B [Pa]	μ [Pa s]	ρ [kg/m ³]	p [Pa] *	u [m/s]
Gas bubble	1.40	0	μ_g	1.2	$p_0 + \Delta p_{g,l}$	0
Tissue/cell	4.04	6.1×10^8	μ_1	1061	$p_0 + \Delta p_{l,c1}$	0
Cell core	4.04	6.1×10^8	μ_2	1061	$p_0 + \Delta p_{c1,c2}$	0
Liquid (preshock)	4.40	6.0×10^8	μ_l	998.6	p_0	0
Liquid (postshock)	4.40	6.0×10^8	μ_l	ρ'	p'	u'

III. PROBLEM SETUP

A. The planar interface configuration

The bubble attached to a planar interface, see configuration (a,i) in Fig. 1(a), corresponds to the experimental setup in Ref. [8] and is used for validation. A mixture of water and 10% solid gelatin [8,9] is employed to mimic the tissuelike material. The resulting acoustic impedance is $1.62 \times 10^6 \text{ kg m}^{-2} \text{ s}^{-1}$, which is similar to that of many human organs, e.g., liver or kidney [26]. The water surrounding the gas bubble near the biomaterial surrogate also has an acoustic impedance of $1.62 \times 10^6 \text{ kg m}^{-2} \text{ s}^{-1}$, and thus all waves are transmitted through the water-tissue interface without reflections. The radius of the gas bubble is $R_0 = 0.8 \text{ mm}$, and the length and width of the domain are $L = 80R_0$ and $W = 8R_0$. Initially, a planar shockwave is located at $H_0 = 1.4R_0$ upstream of the bubble center and propagates upward. Its overpressures, p_s , range from 10.2 to 163.2 MPa,

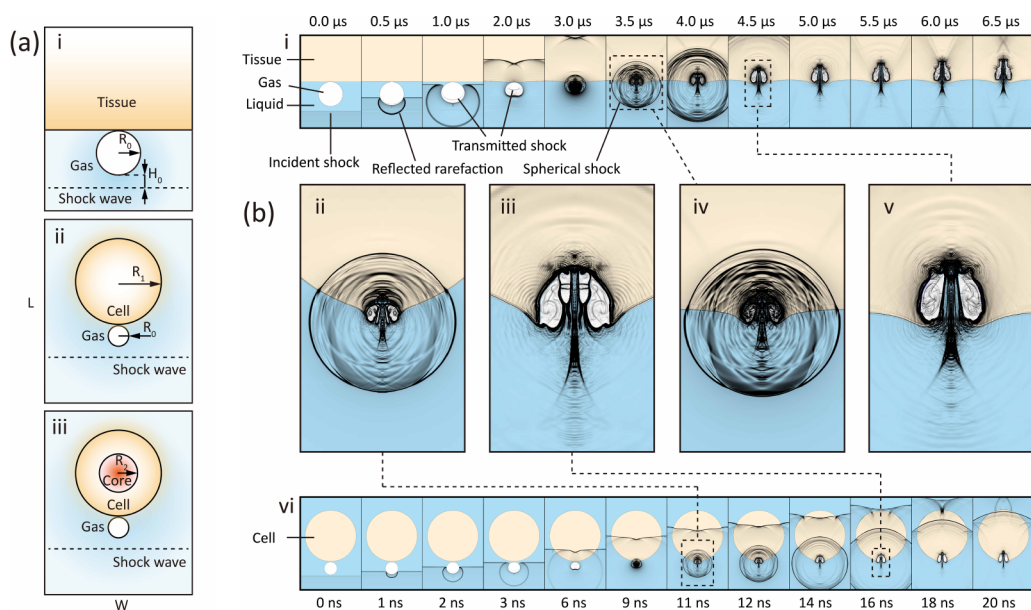


FIG. 1. (a) Considered configurations: (i) planar single interface, (ii) spherical interface, and (iii) spherical two-layer material. Gas bubble, tissue and cell material, cell core, and liquid are colored by white, yellow, red, and blue, respectively. The computational domain size is $L = 80R_0$, $W = 8R_0$; the bubble initial radius is $R_0 = 0.8 \text{ mm}$ for (i) and $R_0 = 2.5 \mu\text{m}$ for (ii) and (iii). (b) Evolution of wave dynamics and hydrodynamics: top row for the planar interface; bottom row for the spherical interface; middle row shows enlarged subsections; wave dynamics is visualized by density-gradient contours. The overpressure for all cases is $p_s = 163.2 \text{ MPa}$ and viscosity is zero.

where the lower bound corresponds to the experiment [8] and the upper bound resembles typical ESWL pressure [10]. The pressure profile, $p'(z) = (p_s - p_0)e^{b(z-60R_0)} + p_0$, where $p_0 = 0.1$ MPa and $b = 393.9 \text{ m}^{-1}$, models laser shock generation [7,8]. The postshock conditions of velocity u' and density ρ' are determined from the Rankine-Hugoniot relation for a given overpressure p_s . We emphasize that the pressure profile and magnitude were chosen in this work for comparison with the reference experiment and may differ from conventional medical therapy settings (tensile part of the pressure wave and moderate amplitudes [27,28]).

The chosen numerical setup (initial conditions, computational domain) and material properties are consistent with the experimental setup [8,9], where the shockwave is generated by laser focusing and the bubble is attached to the gelatin surface using a syringe. An estimation of the Reynolds number and Weber number using the liquid jet velocity u_j at the onset of penetration gives $\text{Re} = \rho_l u_j R_0 / \mu_l \sim \mathcal{O}(10^5)$ and $\text{We} = \rho_l u_j^2 R_0 / \sigma_{g,l} \sim \mathcal{O}(10^7)$, respectively. Clearly, viscous effects as well as surface-tension force effects are considerably smaller as compared to inertial effects and thus can be neglected in this setup.

B. The spherical interface configuration

Unlike with the planar interface, now the diameter of the spherical-drop cell-surrogate model imposes a length scale; see Fig. 1(a,ii). An estimate of Reynolds number as $\mathcal{O}(10)$ to $\mathcal{O}(10^3)$ and of the Weber number as $\mathcal{O}(10^3)$ indicates that viscous and surface-tension effects may no longer be negligible. A gas bubble with initial radius of $R_0 = 2.5 \mu\text{m}$ is positioned at a standoff distance $0.1R_0$ (gap size) near a gelatin bubble of radius $R_1 = 4R_0$. These dimensions resemble realistic parameters (1–5 μm bubble diameters) [11,15,29] and diameters of human embryonic kidney cells of 20–30 μm [11]. The mechanical properties and responses of the cell are modeled by the cortical-shell liquid-drop model [22]. We consider two types of this model. The single liquid-drop model [19] resembles mechanical behavior of leukocytes. The cell has spherical initial shape, Fig. 1(a,ii). The interior is filled by a homogeneous Newtonian liquid, and the cell membrane with its associated cytoskeleton is modeled by an inviscid liquid cortical layer with a constant surface tension coefficient $\sigma_{l,c1}$. We neglect the cortical-layer thickness and set $\sigma_{l,c1} = 2.4 \times 10^{-5} \text{ Nm}^{-1}$ [19]. The viscosity of the cell interior fluid, μ_1 , varies significantly [15]. We investigate μ_1 from 10 to $200\mu_l$, where $\mu_l = 10^{-3} \text{ Pa s}$ is the dynamic viscosity of water at 20°C .

The compound liquid-drop model [20] considers a heterogeneous cell interior which is composed of cytoplasm and nucleus. An infinitely thin layer with constant surface tension $\sigma_{l,c1}$ is used to represent the plasma membrane of width $\sim 0.1 \mu\text{m}$, Fig. 1(a,iii). The endoplasm of the cell is modeled by a Newtonian liquid with viscosity $\mu_1 = 10\mu_l$. The core, representing the nucleus and the surrounding cytoskeleton, is modeled by another spherical liquid drop with a radius of $R_2 = 0.5R_1$ and viscosity μ_2 varying from $2\mu_1$ to $10\mu_1$. The core has a constant cortical tension coefficient $\sigma_{c1,c2} = 2.4 \times 10^{-5} \text{ Nm}^{-1}$ [22,30]. The length and width of the computational domain are $L = 60R_0$ and $W = 10R_0$, respectively. Both drop models are subjected to an incident shockwave with overpressure p_s , initially located at $H_0 = 0.2R_0$ upstream of the bubble center.

IV. NUMERICAL METHOD

A. Governing equations

The dynamics of the fluid phases in the computational domain Ω follow the compressible Navier-Stokes equations. The governing equations are solved for each of the N materials on its domain Ω_r , $r \in [1, N]$ and can be written in short notation as

$$\mathbf{U}_t + \nabla \cdot \mathbf{F}^c + \nabla \cdot \mathbf{F}^v = \mathbf{F}^s + \mathbf{S}(\mathbf{U}). \quad (2)$$

Here, $\mathbf{U} = (\rho, \rho u, \rho v, \rho w, \rho E)^T$ denotes the vector of flow state variables and \mathbf{F}^c , \mathbf{F}^v , and \mathbf{F}^s denote the convective flux tensor, the viscous flux tensor, and the surface-tension source term,

respectively. The geometric source term $\mathbf{S}(\mathbf{U})$ appears under the axisymmetry assumption used in this work.

B. Interface capturing

The multimaterial system is represented by the function $\varphi^\chi(\mathbf{x}) = [\varphi(\mathbf{x}), \chi(\mathbf{x})]$, where $\varphi(\mathbf{x}) > 0$ is the unsigned distance function and $\chi(\mathbf{x}) \in \mathbb{N}$ is the indicator function. The material is labeled by the indicator function and assigned with the respective material properties. The zero-level-set manifold $\Gamma = \{\mathbf{x} | \varphi(\mathbf{x}) = 0\}$ defines the sharp phase interface and is advected with the local fluid velocity. The numerical treatment of the interface evolution follows [31,32]. First, the global level-set function is transformed into multiple local level-set functions by a mapping $\mathbf{C}_m : \mathbb{R} \times \mathbb{N} \rightarrow \mathbb{R}$:

$$\phi^m(\mathbf{x}) = \mathbf{C}_m(\varphi^\chi(\mathbf{x})) = \begin{cases} \varphi(\mathbf{x}) & \text{if } \chi(\mathbf{x}) = m \\ -\varphi(\mathbf{x}) & \text{otherwise} \end{cases}. \quad (3)$$

The resulting N_{ij} level-set functions are then advected from time step n to $n + 1$ by solving the advection equation

$$\phi_t^m + \mathbf{u} \cdot \nabla \phi^m = 0. \quad (4)$$

After advection, a remapping $\mathbf{R} : \mathbb{R}^{N_{ij}} \rightarrow \mathbb{R} \times \mathbb{N}$,

$$\varphi_{ij}^\chi = \mathbf{R}(\phi_{ij}^1, \phi_{ij}^2, \dots, \phi_{ij}^{N_{ij}}) = \left(\max_r \phi_{ij}^r, \arg \max_r \phi_{ij}^r \right) \quad (5)$$

is used to reconstruct the global level-set function [32,33]. Note, for more than two phases present in a computational cell, interface advection is non-trivial since all interactions need to be considered [21]. The interface segments in a multimaterial cell are implicitly defined by the level-set function and can be calculated by geometrical reconstruction.

C. Finite-volume discretization

The computational domain is discretized with a uniform Cartesian grid with constant cell spacing in axial and radial directions. The governing equations are solved on the numerical grid using our recently developed conservative, compressible multimaterial method [21]. This numerical approach allows us to consider multiple immiscible materials that are separated by a sharp interface. Advancing bulk fluid regions is straightforward as a cell is filled with a single phase only. For more complex configurations, the sharp-interface approach can handle so-called cut cells that contain several phases and require special treatment.

The discretized form of the governing equations for each of the phases in a cut cell (i, j) using explicit Euler time marching is given by

$$\alpha_{ij}^{n+1} \mathbf{U}_{ij}^{n+1} = \alpha_{ij}^n \mathbf{U}_{ij}^n + \frac{\Delta t}{h} (A^x \hat{\mathbf{F}}|_{x^-} - A^x \hat{\mathbf{F}}|_{x^+}) + \frac{\Delta t}{h} (A^r \hat{\mathbf{F}}|_{r^-} - A^r \hat{\mathbf{F}}|_{r^+}) + \alpha_{ij}^n \mathbf{S}(\mathbf{U}) + \hat{\mathbf{E}}_{ij}. \quad (6)$$

Here, α_{ij} is the volume fraction of the respective material in this cell (i, j) , Δt is the time step, and h is the uniform grid spacing, respectively. The aperture A denotes the cell face after segmentation by the interface Γ at the current time step. The subscripts (x^-, x^+, r^-, r^+) indicate the cell faces; e.g., x^- and x^+ are the upper and lower axial cell faces, respectively. The last term on the right-hand side of Eq. (6) is the material interaction term [34] and will be discussed in the next section. The vector of conservative states $\alpha_{ij} \mathbf{U}_{ij}$ is defined at the cell center of cell (i, j) for each material, where \mathbf{U}_{ij} is the vector of cell-averaged states. The numerical flux at the cell faces is $\hat{\mathbf{F}} = \hat{\mathbf{F}}^c + \hat{\mathbf{F}}^v$, where the convective numerical flux $\hat{\mathbf{F}}^c$ is interpolated from the physical fluxes using the weighted essentially nonoscillatory scheme [35], and the viscous numerical flux $\hat{\mathbf{F}}^v$ is interpolated by a fourth-order central finite-difference scheme. Time marching is performed by the second-order strong

stability-preserving Runge-Kutta scheme [35] with a time step

$$\Delta t = \mathcal{C} \min \left(\frac{h}{|u| + c}, \frac{h}{|v| + c}, \rho \frac{h^2}{\mu}, \sqrt{\frac{\rho}{8\pi\sigma}} h^{\frac{3}{2}} \right), \quad (7)$$

where c is the speed of sound and $\mathcal{C} = 0.6$.

D. Material interactions

The interaction term $\hat{\mathbf{E}}_{ij}$ in Eq. (6) incorporates the effect of phase interfaces present in the cell (i, j) via

$$\hat{\mathbf{E}}_{ij} = \frac{\Delta t}{h^2} (\hat{\mathbf{E}}_{ij}^v + \hat{\mathbf{E}}_{ij}^c + \hat{\mathbf{E}}_{ij}^s), \quad (8)$$

where the three terms denote viscous, inertial, and surface-tension force effects. We employ the reduced interaction model [21] to simplify the computation of the interactions. In complex multiple-material cells, only the two dominant, i.e., heaviest, phases are considered. Then, the viscous flux across the material interface $\Delta\Gamma^{1,2}$ between two interacting phases 1 and 2 is

$$\hat{\mathbf{E}}_{ij}^v = (0, \hat{\tau} \Delta\Gamma^{1,2} \mathbf{n}, \hat{\tau} \Delta\Gamma^{1,2} \mathbf{n} \cdot \mathbf{u})^T, \quad (9)$$

with the interface viscous stress tensor

$$\hat{\tau} = \hat{\mu} \left(-\frac{2}{3} \nabla \cdot \mathbf{u} \mathbf{I} + (\nabla \mathbf{u} + \nabla \mathbf{u}^T) \right). \quad (10)$$

Following Ref. [23], viscous stress is assumed to be continuous across the interface; thus, the interface viscosity is approximated with

$$\hat{\mu} = \frac{\mu_1 \mu_2}{\alpha_1 \mu_1 + \alpha_2 \mu_2}. \quad (11)$$

Here, μ_m and α_m are the dynamic viscosity and volume fraction of material “m” in the cell (i, j) . Note that the interaction term $\hat{\mathbf{E}}^v$ considers only momentum and energy exchange between connecting materials, while the mass flux is zero due to immiscibility. Similar to the balanced-force formulation [23], we combine the surface-tension interaction $\hat{\mathbf{E}}^s$ and the inertial interaction $\hat{\mathbf{E}}^c$ for the dominant phases $m = 1, 2$ to obtain

$$\hat{\mathbf{E}}_{ij}^{c,m} + \hat{\mathbf{E}}_{ij}^{s,m} = (0, \Delta\Gamma^{1,2} \hat{p}_m \mathbf{n}, \Delta\Gamma^{1,2} \hat{p}_m \mathbf{n} \cdot \hat{\mathbf{u}}_m)^T. \quad (12)$$

The fluid states at the material interface define a constrained Riemann problem [36] with the pressure-jump $\Delta p = \hat{p}_1 - \hat{p}_2 = \sigma_{1,2} \kappa$. This can be solved by the Harten–Lax–van Leer solver with contact restoration [37],

$$\begin{aligned} \hat{u} &= \frac{\rho_2 u_2 \Delta u_2 - \rho_1 u_1 \Delta u_1 + p_1 - p_2 + \sigma_{1,2} \kappa}{\rho_2 \Delta u_2 - \rho_1 \Delta u_1}, \\ \hat{p}_1 &= p_1 + \rho_1 (\hat{u} - u_1) \Delta u_1, \\ \hat{p}_2 &= p_2 + \rho_2 (\hat{u} - u_2) \Delta u_2, \end{aligned} \quad (13)$$

with $\Delta u_1 = s^- - u_1$ and $\Delta u_2 = s^+ - u_2$, where the minimum and maximum wave speeds, s^- and s^+ , are computed following Ref. [38].

E. Parallel computing strategy

A multiresolution representation of the computational grid is employed to achieve high computational efficiency and decrease memory storage. The projection and prediction operators based on cell-averaged values are performed between different resolution levels to compute data on coarser cells from finer cells and vice versa; see Ref. [39] for details. Mesh refinement and coarsening

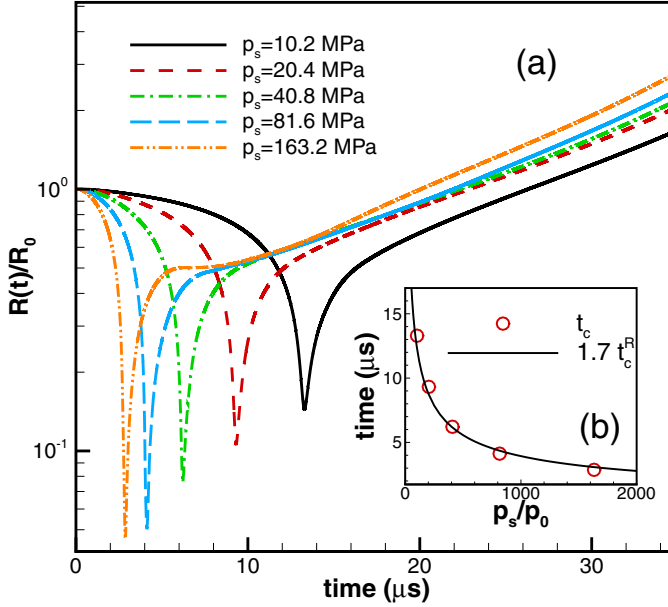


FIG. 2. Time history of the equivalent bubble radius $R(t)$ during the shock-bubble interaction near a tissuelike material for various overpressures p_s (a) and the corresponding bubble collapse time (b). The collapse time, indicated by the minimal equivalent bubble radius, agrees well with the correlation $1.7t_c^R$, where t_c^R is the Rayleigh collapse time [43]. See Movies S1 and S2 of the Supplemental Material [46].

are performed adaptively by comparison of projection and prediction errors with admissible level-dependent thresholds. By design, regions with material interfaces are always discretized with the finest possible resolution level. To further improve computational efficiency, a local time-stepping scheme is applied. Conservation is strictly enforced by conservative flux correction [40]. The parallelization strategy is based on a pyramid data structure and a storage-and-operation-splitting approach [41].

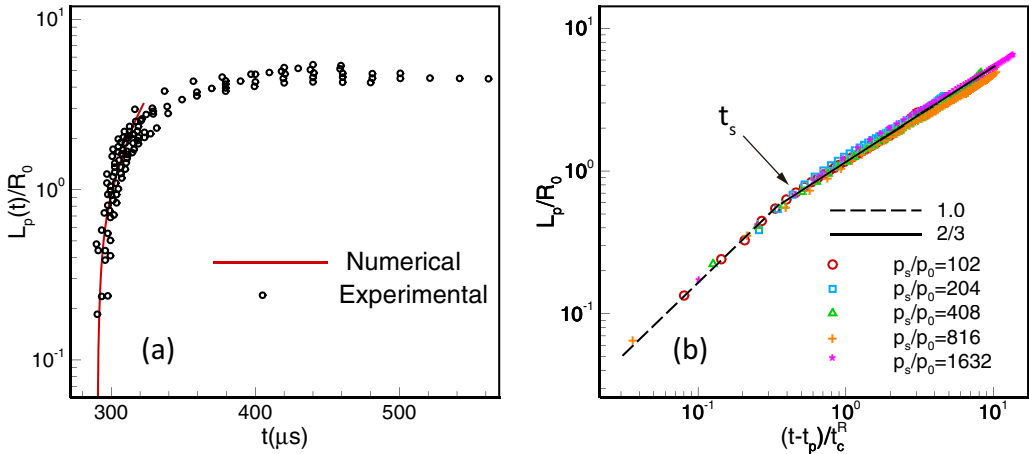


FIG. 3. (a) Time evolution of the penetration compared to the experimental data of Kodama and Takayama [8] for an overpressure of $p_s = 10.2$ MPa. (b) Normalized penetration depth L_p/R_0 vs $(t-t_p)/t_c^R$ for $10.2 \text{ MPa} \leq p_s \leq 163.2 \text{ MPa}$. t_s indicates the transition between two scaling regimes.

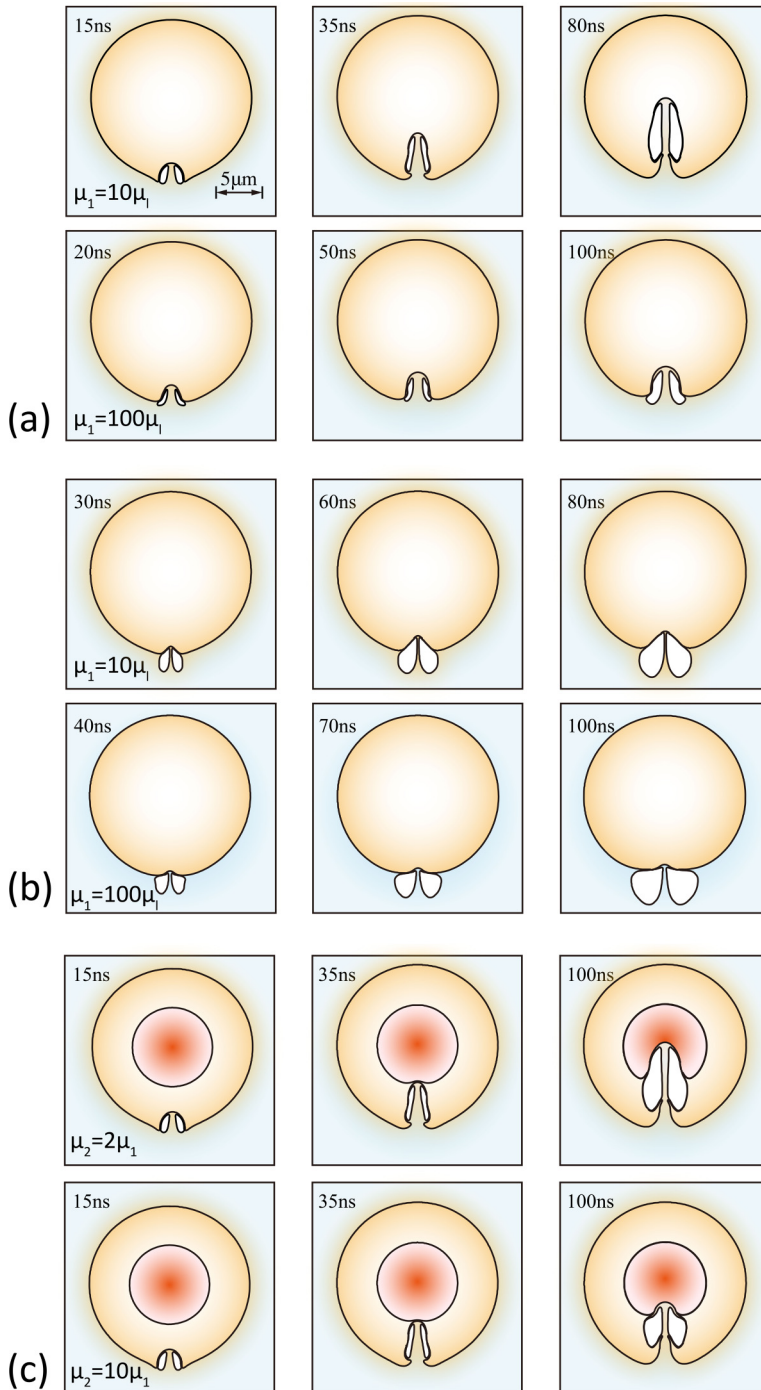


FIG. 4. Interface evolution during bubble-collapse-driven penetration processes for a single cell. Panels (a) and (b) show the single-liquid cell model for high ($p_s = 163.2$ MPa) and low ($p_s = 40.8$ MPa) overpressures, respectively. The results of the compound liquid cell model for high overpressure ($p_s = 163.2$ MPa) are shown in panel (c). See Sec. III and Movie S3 of the Supplemental Material [52].

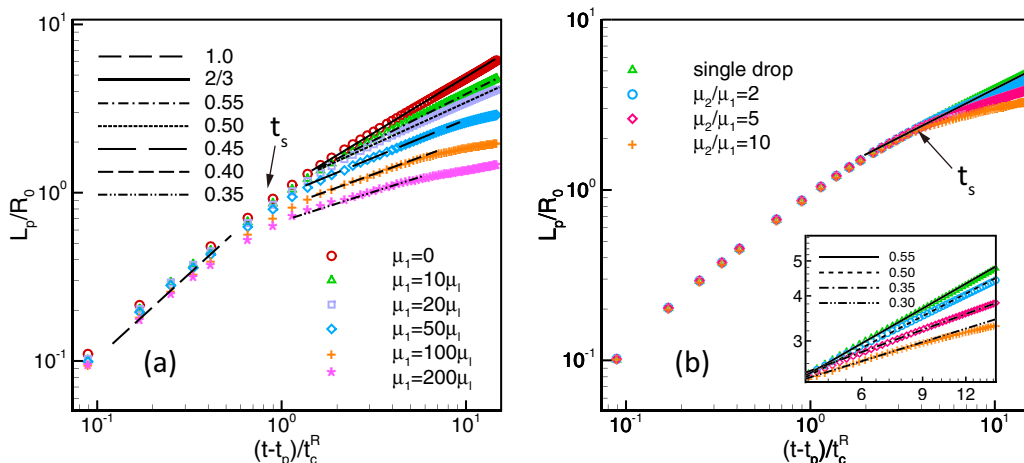


FIG. 5. (a) Penetration-depth evolution for the single-liquid-drop model for various viscosities. (b) Penetration-depth evolution for the compound liquid drop; the outer-layer viscosity is $\mu_1 = 10\mu_l$ and the core viscosity ranges from $\mu_2 = 2\mu_1$ to $10\mu_1$.

V. PENETRATION OF A TISSUELIKE PLANAR MATERIAL INTERFACE

A. Wave dynamics, bubble collapse, and liquid jet formulation

When the initial planar shockwave hits the gas bubble, a transmitted shock and a reflected rarefaction wave [Fig. 1(b,i)] are generated. The high postshock pressure in water induces contraction of the gas bubble and collapse at t_c . The collapse time for $p_s/p_0 = 102$ is $t_c = 13.3 \mu\text{s}$; see Sec. II.A. of the Supplemental Material [42], which agrees very well with the experimental finding of $t_c = 13 \mu\text{s}$; see Fig. 13 of Ref. [8]. After collapse, the gas bubble re-expands or rebounds.

Compared with the Rayleigh collapse time $t_c^R = 0.915\sqrt{\rho_l/(p_s - p_0)}R_0$ [43,44] of a spherical bubble, the collapse time is larger due to the presence of the interface. For a solid interface, it can be estimated as $t_c^R(1 + 0.205R_0/d)$ [45], where d is the standoff distance, i.e., $d = R_0$ for an attached bubble. For a tissue-like material, we measure the collapse time by the equivalent bubble radius $R(t)$, Fig. 2(a). It is fitted by $t_c = 1.7t_c^R$ which is larger than for a solid interface, Fig. 2(b). Note that at $t \geq 2.0 \mu\text{s}$, the shockwave travels into the gelatin without visible reflection, Fig. 1(b,i).

Another important feature is the development of a re-entrant liquid jet [47–49] in shock-propagation direction. Once this jet splits the bubble, a water-hammer shock is emitted [50]; see $t = 3.5 \mu\text{s}$ in Fig. 1(b,i). The jet strikes the gelatin interface and increases the surface pressure significantly [6,7]. Subsequently, small-scale baroclinic vorticity deposition occurs at the gel interface, which is visible in Fig. 1(b,ii). The gelatin surface initially migrates toward the gas bubble due to the sink flow generated by the collapsing bubble. With increasing overpressure of the initial shockwave, this migration is smaller, as the collapse time decreases and the sink flow becomes less effective at the interface; see Fig. 3 of the Supplemental Material for a series of snapshots [51].

B. Dynamics of the penetration process

Good agreement is obtained with experimental data [8] for penetration depths up to $L_p \simeq 2R_0$, Fig. 3(a). As for the simulation inviscid fluid was assumed, the agreement shows that the early stages of the penetration process are inertia dominated. Elastic effects due to the gelatin material, which dampen penetration in the experiment at late times, cannot be reproduced by the numerical model. Thus the numerical result deviates from experimental data from $t \simeq 320 \mu\text{s}$ in Fig. 3(a).

Figure 3(b) shows the penetration-depth evolution for different overpressures p_s/p_0 . Here, t_p defines the onset of penetration as the time instant when the interface ceases upstream motion

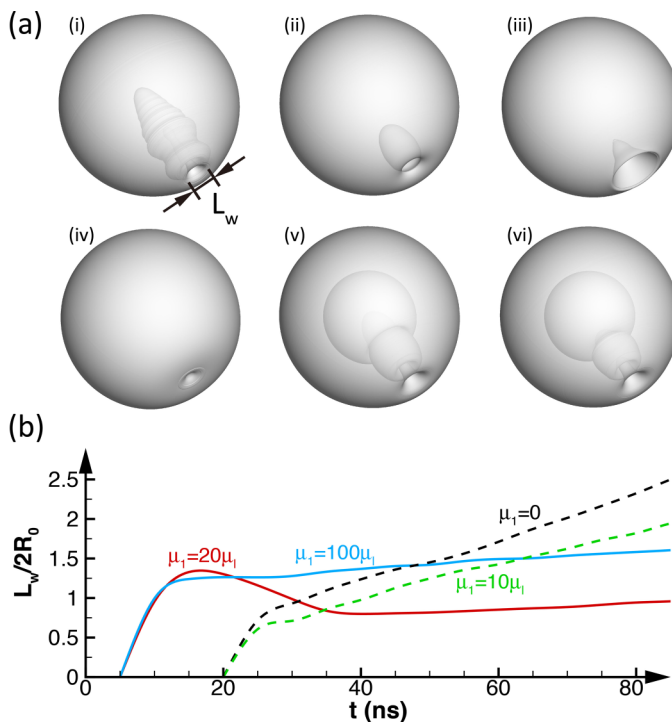


FIG. 6. (a) Perforation diameter L_w for the single drop model [(i)–(iv)] and the compound drop model [(v) and (vi)]. At $p_s = 163.2$ MPa, the viscosities are $\mu_1 = 10\mu_l$ and $\mu_1 = 100\mu_l$ for (a, i) ($t = 80$ ns) and (a, ii) ($t = 100$ ns), respectively. Accordingly, panels (iii) and (iv) show the interface for low overpressure $p_s = 40.8$ MPa. The pit diameter L_w is shown in panel (b) for the single-drop model at $p_s = 163.2$ MPa (solid line) and $p_s = 40.8$ MPa (dashed line).

due to bubble-sink effect and starts to move in downstream (shock-propagation) direction. For the inviscid flow model two regimes develop, the first with linear scaling in time and the subsequent with $t^{2/3}$ scaling. Note that although here we are solving the Euler equation, which is scale free, the employed shock-capturing numerical method inevitably introduces numerical viscosity which may be the reason that the penetration rate deviates from the linear scaling profile.

VI. PENETRATION OF A SINGLE CELL

A. Dynamics of single-cell penetration

An overview of the bubble-collapse and cell-penetration process is given in Fig. 1(b,vi) for an overpressure of $p_s = 163.2$ MPa following Ref. [10]. The bubble collapse is complete within a few nanoseconds; see the convergence study in the Supplemental Material [53]. A clear effect of viscosity can be observed for the interface evolution, Fig. 4(a). For $\mu_1 \leq 50\mu_l$, the deformed bubble is totally absorbed by the cell, while for $\mu_1 = 100\mu_l$, the bubble penetrates only partially into the cell. For a weaker incident shockwave of $p_s = 40.8$ MPa, bubble absorption is strongly reduced, up to negligible penetration for increasing viscosity, Fig. 4(b). The effect of viscosity on the penetration depth is shown in Fig. 5(a). The linear regime exists for all parameters, followed by a sublinear regime after the transition time $t_s = t - t_p \sim t_c^R$. Viscosity reduces the slope of the power-law regime as compared to the inviscid case.

For the compound liquid drop model, Fig. 1(a,iii), the heterogeneous cell interior affects the late stage of the penetration dynamics. The interface evolution at $t = 15, 35$, and 100 ns in Fig. 4(c)

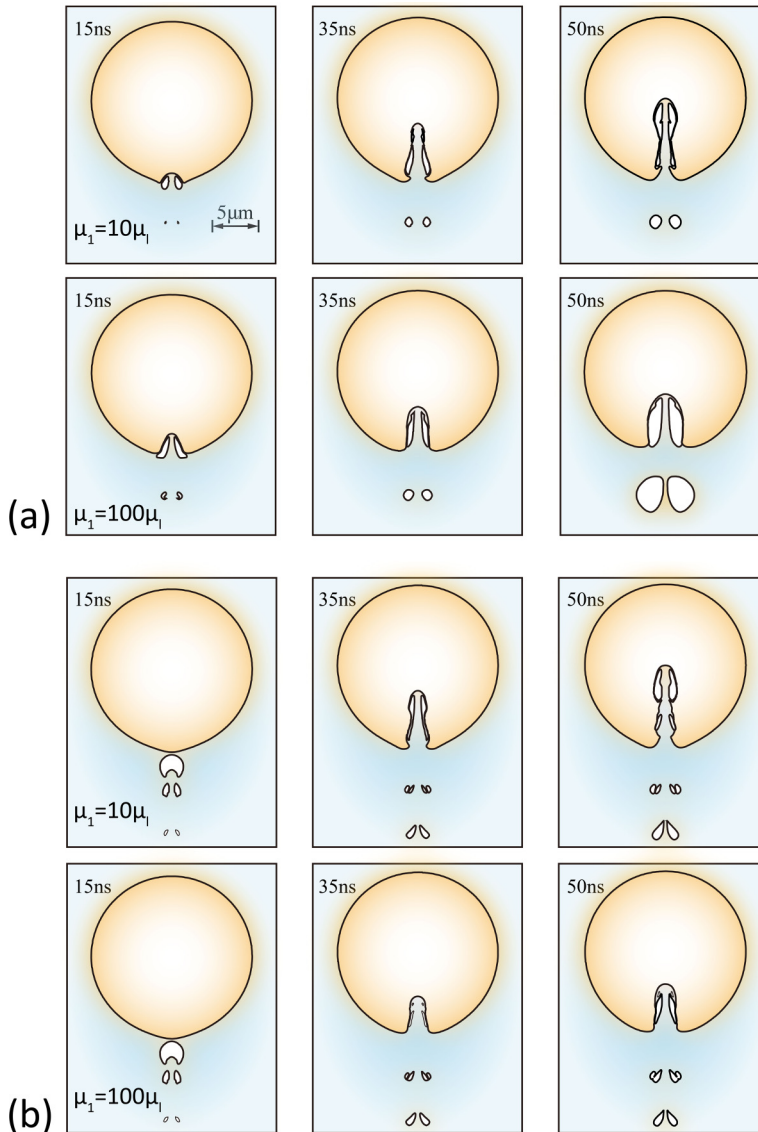


FIG. 7. Interface evolution during bubble-collapse-driven penetration processes for a single cell and multiple microbubbles [two bubbles in panel (a) and three bubbles in panel (b)] under a large overpressure ($p_s = 163.2$ MPa). See Sec. V and Movie S4 of the Supplemental Material [58].

reveals that the penetration behavior remains the same as for the single liquid drop before the liquid jet impacts the core. After the impact at $t = 35$ ns, penetration is damped by interaction with the core. Figure 5(b) indicates three different stages of the penetration. The first and second ones are the same as for the single liquid drop model. After jet impacts on the core, a third stage with decelerated penetration is observed; see the insert of Fig. 5(b).

B. The damage pit

To understand the mechanical effects during bubble-collapse-driven penetration of biomaterial-surrogate liquid-liquid interfaces, we analyze the damage pit of the cell model due to penetration.

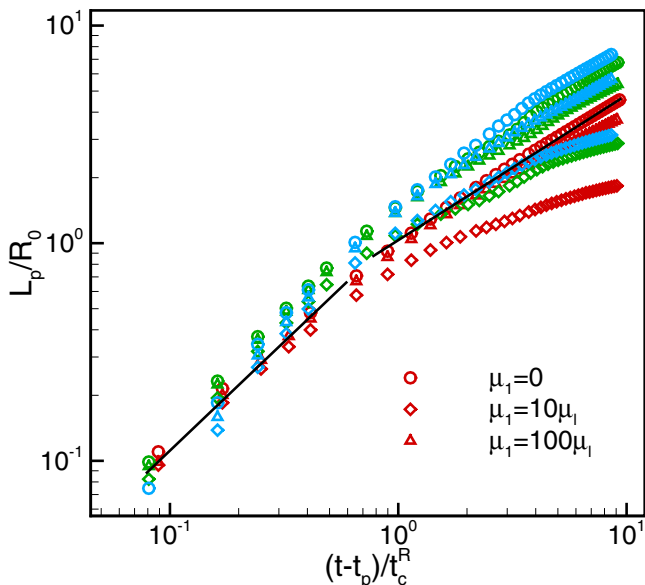


FIG. 8. Time history of penetration depth for the shock-single-cell interaction problem for the single-liquid-drop model and a microbubble array. The red, green, and blue symbols refer to the penetration with single, double, and triple microbubbles. The solid lines indicate the power laws 1.0 and $2/3$.

Figure 6(a) shows three-dimensional surface visualizations of the cell models. Differences are observed depending on the cell model, viscosity, and shock strength. The damage effect on the cell is quantified by the pit diameter L_w of the perforation, Fig. 6(b). Two different types are observed: a relatively constant hole punch and a continuously growing orifice. The pit of the single-liquid-drop model with high overpressure $p_s = 163.2$ MPa develops an almost constant diameter for viscosity μ_1 smaller than $50\mu_l$, Figs. 6(a,i) and 6(b). After a maximum diameter of $L_w \sim 1.4R_0$ at $t = 15$ ns, a stationary size of approximately $0.8R_0$ is assumed, because the high-speed jet advects the collapsed gas bubble entirely into the cell without further radial acceleration of the orifice. For low overpressure, Figs. 6(a,iii) and 6(a,iv), or at sufficiently high liquid viscosity, Fig. 6(a,ii), the collapsed bubble only partly penetrates the cell. As the remaining gas volume outside the cell further expands, shear forces at the cell membrane widen the damage pit.

C. The effect of bubble arrays

In real applications, the target materials encounter complex penetration patterns when exposed to large number of microbubbles with different sizes [54,55]. To mimic collapsing bubble arrays, we study the effect of an equal-size bubble column. The interface evolution for low-viscous and high-viscous single-liquid cells with two and three microbubbles is shown in Figs. 7(a) and 7(b), respectively. For more snapshots, we refer the reader to the Supplemental Material [56]. Overall, penetration is enhanced. The water-hammer shock waves and multiple liquid jets cause complex wave interactions and amplification of penetration effects. This indicates an enhancement of the energy focusing by multiple microbubbles. As shown in a previous study [57], bubbles mainly interact with the collapse-induced shocks of upstream bubbles, which have increasing intensity. The cell-penetrating liquid jet accumulates momentum leading to increased penetration depths at smaller time scales, Fig. 7(b). This observation is confirmed by the penetration evolution, Fig. 8. Unlike the constant regime for the single bubble collapse, Fig. 5, the initial stage of multiple bubble-driven penetration exhibits an acceleration, followed by a deceleration at later times. The general damping effect of viscosity is similar. For weak shocks, enhancement still can be observed. However, due

to the larger sink flow effect by multiple upstream bubbles, the nearest bubble moves further away from the interface at the beginning of interaction, partially counteracting the enhanced liquid jet.

VII. CONCLUSIONS AND OUTLOOKS

We have presented a numerical investigation of bubble-collapse-driven penetration at biomaterial-surrogate liquid-liquid interfaces. For a generic setting, the effects of single- and multiple-bubble-collapse dynamics on the penetration of cells due to shockwave interaction were investigated. The tissue material is modeled as gelation and considered as a fluid phase in the simulations. We have shown that depending on the strength of the initial shockwave, the bubble can penetrate the tissuelike gelatin phase prior to maximal compression. At the same time, the strength and width of the liquid jet increase and lead to larger ambient fluid entrainment into the gelatine material. A quantitative comparison of the penetration depth with experimental data from literature shows very good agreement. We found two scaling regimes for the penetration depth as a function of postcollapse time in inertia-dominated configurations. Interestingly, for strong shocks and low-viscous gel material, the penetration diameter reaches an almost constant size. Weak overpressures, however, result in a continuous widening of the radial pore size. In further investigations we want to focus on this pore size effect to explore its connection to the resealing capability of viable cells after sonoporation. Unlike with experiments, full field quantitative data can be extracted to analyze physical mechanisms that can be harnessed for steering the penetration process. Investigations of the liquid jet in combination with more complex and more realistic material models help to further improve biomedical exploitation and are the focus of our ongoing research. The current work is limited to simple configurations of the bubble-collapse-driven penetration process and to simplified surrogate models of biomaterials. We note that the next step has to include refined material models by incorporating elastic and plastic effects. This will reduce the modeling error for the late stage of the penetration process, as shown in Fig. 3(a). Also, future work will concentrate on fully three-dimensional bubble array simulations allowing for more realistic nonaxisymmetric bubble distributions as found in sonoporation and ESWL.

ACKNOWLEDGMENTS

This project has received funding from the European Research Council (ERC) under the European Union's Horizon 2020 research and innovation programme (Grant Agreement No. 667483). Parts of the results in this work were obtained during the CTR Summer Program 2016. The authors gratefully acknowledge the Gauss Centre for Supercomputing e.V. for funding this project by providing computing time on the GCS Supercomputer SuperMUC at Leibniz Supercomputing Centre.

-
- [1] F. Yuan, C. Yang, and P. Zhong, Cell membrane deformation and bioeffects produced by tandem bubble-induced jetting flow, *Proc. Natl. Acad. Sci. USA* **112**, E7039 (2015).
 - [2] J. E. Lingeman, J. A. McAteer, E. Gnessin, and A. P. Evan, Shock wave lithotripsy: Advances in technology and technique, *Nat. Rev. Urol.* **6**, 660 (2009).
 - [3] C. C. Coussios and R. A. Roy, Applications of acoustics and cavitation to noninvasive therapy and drug delivery, *Annu. Rev. Fluid Mech.* **40**, 395 (2008).
 - [4] M. O. Steinhauser and M. Schmidt, Destruction of cancer cells by laser-induced shock waves: Recent developments in experimental treatments and multiscale computer simulations, *Soft Matter* **10**, 4778 (2014).
 - [5] J. B. Freund, R. K. Shukla, and A. P. Evan, Shock-induced bubble jetting into a viscous fluid with application to tissue injury in shock-wave lithotripsy, *J. Acoust. Soc. Am.* **126**, 2746 (2009).

- [6] E. Johnsen and T. Colonius, Numerical simulations of non-spherical bubble collapse, *J. Fluid Mech.* **629**, 231 (2009).
- [7] K. Kobayashi, T. Kodama, and H. Takahira, Shock wave-bubble interaction near soft and rigid boundaries during lithotripsy: Numerical analysis by the improved ghost fluid method, *Phys. Med. Biol.* **56**, 6421 (2011).
- [8] T. Kodama and K. Takayama, Dynamic behavior of bubbles during extracorporeal shock-wave lithotripsy, *Ultrasound Med. Biol.* **24**, 723 (1998).
- [9] T. Kodama and Y. Tomita, Cavitation bubble behavior and bubble-shock wave interaction near a gelatin surface as a study of in vivo bubble dynamics, *Appl. Phys. B* **70**, 139 (2000).
- [10] A. M. Loske, The role of energy density and acoustic cavitation in shock wave lithotripsy, *Ultrasonics* **50**, 300 (2010).
- [11] Z. Fan, H. Liu, M. Mayer, and C. X. Deng, Spatiotemporally controlled single cell sonoporation, *Proc. Natl. Acad. Sci. USA* **109**, 16486 (2012).
- [12] T. D. Khokhlova, Y.-N. Wang, J. C. Simon, B. W. Cunitz, F. Starr, M. Paun, L. A. Crum, M. R. Bailey, and V. A. Khokhlova, Ultrasound-guided tissue fractionation by high intensity focused ultrasound in an *in vivo* porcine liver model, *Proc. Natl. Acad. Sci. USA* **111**, 8161 (2014).
- [13] C.-D. Ohl, M. Arora, R. Iking, N. de Jong, M. Versluis, M. Delius, and D. Lohse, Sonoporation from jetting cavitation bubbles, *Biophys. J.* **91**, 4285 (2006).
- [14] P. Prentice, A. Cuschieri, K. Dholakia, M. Prausnitz, and P. Campbell, Membrane disruption by optically controlled microbubble cavitation, *Nat. Phys.* **1**, 107 (2005).
- [15] W. Zhong, W. H. Sit, J. M. Wan, and A. C. Yu, Sonoporation induces apoptosis and cell cycle arrest in human promyelocytic leukemia cells, *Ultrasound Med. Biol.* **37**, 2149 (2011).
- [16] E.-A. Brujan, K. Nahen, P. Schmidt, and A. Vogel, Dynamics of laser-induced cavitation bubbles near an elastic boundary, *J. Fluid Mech.* **433**, 251 (2001).
- [17] V. Coralic and T. Colonius, Shock-induced collapse of a bubble inside a deformable vessel, *Eur. J. Mech. B Fluids* **40**, 64 (2013).
- [18] N. Hawker and Y. Ventikos, Interaction of a strong shockwave with a gas bubble in a liquid medium: A numerical study, *J. Fluid Mech.* **701**, 59 (2012).
- [19] A. Yeung and E. Evans, Cortical shell-liquid core model for passive flow of liquid-like spherical cells into micropipets, *Biophys. J.* **56**, 139 (1989).
- [20] R. Hochmuth, H. Ting-Beall, B. Beatty, D. Needham, and R. Tran-Son-Tay, Viscosity of passive human neutrophils undergoing small deformations, *Biophys. J.* **64**, 1596 (1993).
- [21] S. Pan, L. Han, X. Hu, and N. A. Adams, A conservative interface-interaction method for compressible multi-material flows, *J. Comput. Phys.* **371**, 870 (2018).
- [22] C. Lim, E. Zhou, and S. Quek, Mechanical models for living cells: A review, *J. Biomech.* **39**, 195 (2006).
- [23] J. Luo, X. Hu, and N. A. Adams, A conservative sharp interface method for incompressible multiphase flows, *J. Comput. Phys.* **284**, 547 (2015).
- [24] M. L. Calvisi, J. I. Ilroeta, and A. J. Szeri, Dynamics of bubbles near a rigid surface subjected to a lithotripter shock wave. Part 2. Reflected shock intensifies non-spherical cavitation collapse, *J. Fluid Mech.* **616**, 63 (2008).
- [25] R. Menikoff and B. J. Plohr, The Riemann problem for fluid flow of real materials, *Rev. Mod. Phys.* **61**, 75 (1989).
- [26] S. Goss, R. Johnston, and F. Dunn, Comprehensive compilation of empirical ultrasonic properties of mammalian tissues, *J. Acoust. Soc. Am.* **64**, 423 (1978).
- [27] C. C. Church, A theoretical study of cavitation generated by an extracorporeal shock wave lithotripter, *J. Acoust. Soc. Am.* **86**, 215 (1989).
- [28] E. Johnsen and T. Colonius, Shock-induced collapse of a gas bubble in shockwave lithotripsy, *J. Acoust. Soc. Am.* **124**, 2011 (2008).
- [29] B. Helfield, X. Chen, S. C. Watkins, and F. S. Villanueva, Biophysical insight into mechanisms of sonoporation, *Proc. Natl. Acad. Sci. USA* **113**, 9983 (2016).
- [30] H.-C. Kan, H. Udaykumar, W. Shyy, and R. Tran-Son-Tay, Hydrodynamics of a compound drop with application to leukocyte modeling, *Phys. Fluids* **10**, 760 (1998).

- [31] S. Osher and J. A. Sethian, Fronts propagating with curvature-dependent speed: Algorithms based on Hamilton-Jacobi formulations, *J. Comput. Phys.* **79**, 12 (1988).
- [32] S. Pan, X. Hu, and N. A. Adams, High-resolution method for evolving complex interface networks, *Comput. Phys. Commun.* **225**, 10 (2018).
- [33] S. Pan, X. Lyu, X. Y. Hu, and N. A. Adams, High-order time-marching reinitialization for regional level-set functions, *J. Comput. Phys.* **354**, 311 (2018).
- [34] X. Hu, B. Khoo, N. A. Adams, and F. Huang, A conservative interface method for compressible flows, *J. Comput. Phys.* **219**, 553 (2006).
- [35] D.-W. Shu and S. Osher, Efficient implementation of essentially non-oscillatory shock-capturing schemes, *J. Comput. Phys.* **77**, 439 (1988).
- [36] D. P. Garrick, M. Owkes, and J. D. Regele, A finite-volume HLLC-based scheme for compressible interfacial flows with surface tension, *J. Comput. Phys.* **339**, 46 (2017).
- [37] E. F. Toro, M. Spruce, and W. Speares, Restoration of the contact surface in the HLL-Riemann solver, *Shock Waves* **4**, 25 (1994).
- [38] X. Hu, N. Adams, and G. Iaccarino, On the HLLC Riemann solver for interface interaction in compressible multi-fluid flow, *J. Comput. Phys.* **228**, 6572 (2009).
- [39] A. Harten, Multiresolution algorithms for the numerical solution of hyperbolic conservation laws, *Commun. Pure Appl. Math.* **48**, 1305 (1995).
- [40] M. O. Domingues, S. M. Gomes, O. Roussel, and K. Schneider, An adaptive multiresolution scheme with local time stepping for evolutionary pdes, *J. Comput. Phys.* **227**, 3758 (2008).
- [41] L. Han, X. Hu, and N. A. Adams, Adaptive multi-resolution method for compressible multi-phase flows with sharp interface model and pyramid data structure, *J. Comput. Phys.* **262**, 131 (2014).
- [42] See Supplemental Material at <http://link.aps.org/supplemental/10.1103/PhysRevFluids.3.114005> for a validation of the free-field bubble collapse in Fig. 2 of Sec. II A.
- [43] C. E. Brennen, *Cavitation and Bubble Dynamics* (Cambridge University Press, Cambridge, UK, 2013).
- [44] L. Rayleigh, VIII. On the pressure developed in a liquid during the collapse of a spherical cavity, *Philos. Mag.* **34**, 94 (1917).
- [45] A. Vogel and W. Lauterborn, Acoustic transient generation by laser-produced cavitation bubbles near solid boundaries, *J. Acoust. Soc. Am.* **84**, 719 (1988).
- [46] See Supplemental Material at <http://link.aps.org/supplemental/10.1103/PhysRevFluids.3.114005> for Movies S1 and S2 showing an animated interface evolution of a single bubble collapse near a tissue-like material.
- [47] J. R. Blake and D. C. Gibson, Cavitation bubbles near boundaries, *Annu. Rev. Fluid Mech.* **19**, 99 (1987).
- [48] A. Philipp and W. Lauterborn, Cavitation erosion by single laser-produced bubbles, *J. Fluid Mech.* **361**, 75 (1998).
- [49] M. S. Plesset and A. Prosperetti, Bubble dynamics and cavitation, *Annu. Rev. Fluid Mech.* **9**, 145 (1977).
- [50] C. Ohl and R. Ikink, Shock-Wave-Induced Jetting of Micron-Size Bubbles, *Phys. Rev. Lett.* **90**, 214502 (2003).
- [51] See Supplemental Material at <http://link.aps.org/supplemental/10.1103/PhysRevFluids.3.114005> for a visualization of the interface topology during bubble collapse near a planar tissue-like material interface in Fig. 3.
- [52] See Supplemental Material at <http://link.aps.org/supplemental/10.1103/PhysRevFluids.3.114005> for the Movie S3 showing an animated interface evolution of the compound liquid cell model.
- [53] See Supplemental Material at <http://link.aps.org/supplemental/10.1103/PhysRevFluids.3.114005> for a convergence study of the temporal equivalent bubble radius evolution in Sec. III.
- [54] D. Fuster and T. Colonius, Modelling bubble clusters in compressible liquids, *J. Fluid Mech.* **688**, 352 (2011).
- [55] D. Rossinelli, B. Hejazialhosseini, P. Hadjidoukas, C. Bekas, A. Curioni, A. Bertsch, S. Futral, S. J. Schmidt, N. A. Adams, and P. Koumoutsakos, 11 pfl/s simulations of cloud cavitation collapse, in *SC '13: Proceedings of the International Conference on High Performance Computing, Networking, Storage and Analysis* (IEEE, Denver, Colorado, 2013), pp. 1–13.

- [56] See Supplemental Material at <http://link.aps.org/supplemental/10.1103/PhysRevFluids.3.114005> for a visualization of the interface evolution during bubble-array-collapse-driven penetration processes of a single cell in Sec. V, see Refs. [59–63].
- [57] E. Lauer, X. Hu, S. Hickel, and N. A. Adams, Numerical investigation of collapsing cavity arrays, *Phys. Fluids* **24**, 052104 (2012).
- [58] See Supplemental Material at <http://link.aps.org/supplemental/10.1103/PhysRevFluids.3.114005> for the Movie S4 showing an animated interface evolution of a bubble-array collapse scenario.
- [59] N. Apazidis, Numerical investigation of shock induced bubble collapse in water, *Phys. Fluids* **28**, 046101 (2016).
- [60] J. Li, Y. Y. Renardy, and M. Renardy, A numerical study of periodic disturbances on two-layer Couette flow, *Phys. Fluids* **10**, 3056 (1998).
- [61] S. Pan, X. Hu, and N. A. Adams, A consistent analytical formulation for volume estimation of geometries enclosed by implicitly defined surfaces, *SIAM J. Sci. Comput.* **40**, A1523 (2018).
- [62] M. Sussman, P. Smereka, and S. Osher, A level set approach for computing solutions to incompressible two-phase flow, *J. Comput. Phys.* **114**, 146 (1994).
- [63] H. Zhou and C. Pozrikidis, The flow of suspensions in channels: Single files of drops, *Phys. Fluids A: Fluid Dyn.* **5**, 311 (1993).